crystals

MDPI

Article

Electronic Properties and Chemical Bonding in V_2FeSi and Fe_2VSi Heusler Alloys

Aisulu Abuova [1], Nurpeiis Merali [1], Fatima Abuova [1], Vladimir Khovaylo [2,3], Nursultan Sagatov [4,*] and Talgat Inerbaev [1,2,*]

[1] Department of Technical Physics, International Department of Nuclear Physics, New Materials and Technologies, L.N. Gumilyov Eurasian National University, Astana 010008, Kazakhstan
[2] Department of Functional Nanosystems and High-Temperature Materials, National University of Science and Technology "MISIS", 119049 Moscow, Russia
[3] Laboratory for Thermoelectric Materials and Structures, Belgorod State University, 308015 Belgorod, Russia
[4] Department of Geology and Geophysics, Novosibirsk State University, 630090 Novosibirsk, Russia
* Correspondence: sagatinho23@gmail.com (N.S.); talgat.inerbaev@gmail.com (T.I.); Tel.: +7-952-940-3247 (N.S.); +7-775-742-6208 (T.I.)

Abstract: First-principles calculations of the stability, electronic, and magnetic properties of full-Heusler compounds V_2FeSi and Fe_2VSi in regular ($L2_1$) and inverse (XA) structures have been performed using density functional theory within an SCAN meta-GGA functional. It is found that the XA crystal lattice is energetically more favorable for V_2FeSi, while Fe_2VSi forms the $L2_1$ structure. In both cases, the electronic structure of the energetically stable modifications corresponds to half-metallic ferrimagnets. Magnetic properties of energetically favorable structures obey the Slater–Pauling rule. All considered properties of the studied structures are explained within the crystal orbital Hamilton population analysis.

Keywords: Heusler alloy; structural ordering; density functional theory; electronic structure; COHP

check for updates

Citation: Abuova, A.; Merali, N.; Abuova, F.; Khovaylo, V.; Sagatov, N.; Inerbaev, T. Electronic Properties and Chemical Bonding in V_2FeSi and Fe_2VSi Heusler Alloys. *Crystals* **2022**, *12*, 1546. https://doi.org/10.3390/cryst12111546

Academic Editors: Weiwei Zhou and Huakang Bian

Received: 6 October 2022
Accepted: 26 October 2022
Published: 29 October 2022

1. Introduction

Heusler alloys are intermetallic compounds with a wide range of compositions attracting much attention due to their potential applications as thermoelectric, spintronic, and magnetostrictive materials. The structural, electronic, thermodynamic, and magnetic properties of many Heusler compounds have previously been studied experimentally [1–11] and theoretically [12–22]. Some of the Heusler alloys are half-metals with 100% spin polarization and high structural stability that is critically important for spintronic applications [12].

Spintronics and magnetoelectronics compose one of the most rapidly expanding fields in nanoscience [23–25]. Half-metallic magnetic compounds play a crucial role in this development. These materials present usual metallic behavior for the one-spin direction, while an energy gap in the band structure is present in the other spin direction similarly to semiconductors. The interest in these compounds is not least due to the fact that the properties of complete Heusler alloys strongly depend on their structure and composition.

Thirty years ago, Nishino et al. [4] investigated the Heusler connection of Fe_3Si with a cubic structure $D0_3$ and $(Fe_{1-x}M_x)_3Si$, (M = Ti, V, Cr, Mn, Co, and Ni) using electrical resistance and reported that the ferromagnetic transition occurs in the range $0 \leq x \leq 0.2$ for M = V. When studying the thermodynamic properties of the Heusler compound $(Fe_{1-x}V_x)_3Si$ with a $D0_3$ structure, $(0 \leq x \leq 0.2)$, it was suggested that the atomic disorder of the V position by Fe atoms leads to the appearance of magnetic frustration [6]. An experimental study of the magnetic properties of Heusler alloys based on Fe_2VSi showed that Fe_2VSi exhibits ferromagnetism with a slight substitution of V by magnetic transition metals [7]. Photoemission spectroscopy was used to study the electronic structures of compounds of Heusler type $Fe_{3-x}V_xSi$ in the concentration range of $0 \leq x \leq 1$.

As the vanadium concentration increases, the crystal structure of $Fe_{3-x}V_xSi$ changes from $D0_3$ to $L2_1$ in the concentration range $0 \leq x \leq 1$ [26]. Photoemission spectroscopy studies show that Fe_2VSi alloy has a pseudogap near the Fermi level at $x \approx 1$ [8].

An early theoretical modeling of the electronic properties of $Fe_2V_{1-x}Cr_xSi$ (x = 0, 0.5, 1.0) employing the FP-LAPW method with the PBEsol functional showed that alloys Fe_2VSi do not exhibit half-metallicity [21]. LMTO-ASA band structure calculations were performed for paramagnetic (PM), ferromagnetic (FM), and antiferromagnetic (AFM) orderings of Fe_2VSi alloys [22]. It was found that AFM ordering is the most stable configuration. As for the magnetic moments, they slightly increase on Fe atoms from FM to AFM. The result for $(Fe_{15/16}V_{1/16})_2(V_{7/8}Fe_{1/8})Si$ indicates the possibility of the existence of Fe atoms with large magnetic moments due to atomic disorder between the Fe and V atoms [22]. The AFM nature of the ordering in Fe_2VSi was confirmed by experimental studies, where a negative value of the Weiss temperature was obtained [6].

Here, we perform a comparative study of the properties of V_2FeSi and Fe_2VSi Heusler alloys for both $L2_1$ and XA structures to identify the origins responsible for the formation of various crystal structures. In addition, this study aims to examine the properties of Heusler alloys from the perspective of the local environment and to analyze their impact on the magnetic and electronic properties. It should be noted that to the best of our knowledge, there are no available experimental data on the properties of V_2FeSi alloys, and one theoretical research paper mentioned this compound among other full Heusler alloys [18].

2. Materials and Methods

The electronic structure calculations were performed within the density functional method implemented in the VASP software package [27–29]. Core electrons were approximated using projector augmented wave (PAW) pseudopotentials [30], and valence electrons were represented with a set of plane wave basis with a cutoff energy of 700 eV. The exchange–correlation functional was treated using SCAN (meta-GGA) [31]. The valence configurations have been chosen as Mn ($3d^64s^1$), Fe ($3d^64s^2$), V ($3d^44s^1$), and Si ($3s^23p^2$). The Brillouin zone was sampled using a Monkhorst–Pack [32] k-point mesh of $10 \times 10 \times 10$. These parameters ensured good convergence in total energy. The convergence tolerance for the calculations was chosen as the difference in total energy within 10^{-7} eV/atom.

The formation enthalpy was calculated by the formula:

$$\Delta H(X_2YZ) = H(X_2YZ)/N - [2H(X) + H(Y) + H(Z)]$$

where H is the enthalpy of each component (X = V, Fe; Y = Fe, V; Z = Si), and N is the number of formula units (f.u.) in a unit cell. A negative ΔH indicates that a structure is stable relative to the decomposition into constituent elements.

The non-empirical strongly constrained and appropriately normed (SCAN) meta-generalized gradient approximation (meta-GGA) within the density functional theory predicts accurate geometries and energies of diversely bonded molecules and materials (including covalent, metallic, ionic, hydrogen, and van der Waals bonds) [31,33]. The computational cost of hybrid functionals can be 10 or 100 times greater than for semi-local functionals in standard plane-wave codes, especially for metallic systems. Another problem with hybrids is that a universal exact-exchange mixing parameter is not determined by any exact condition.

To analyze the nature of chemical bonding in the considered structures, a crystal orbital Hamilton population analysis (COHP) was used [34–36]. According to this formalism, the formation of anti-bonding orbitals occurs when the COHP value taken with the opposite sign becomes negative. We also use the integrated crystal orbital Hamilton population (ICOHP) to measure the strength of the chemical bonding and explain the differences in the stability of crystal structures and the values of atomic magnetic moments.

Atomic structures were visualized in the VESTA package [37]. We use the VASPKIT code to postprocess the calculated data from VASP [38].

3. Results

Atoms in the structures of Heusler alloys X_2YZ (X, Y are transition metals, Z is a chemical element of the main group) are located in four different sites A, B, C and D with coordinates (0, 0, 0), (0.25, 0.25, 0.25), (0.5, 0.5, 0.5), and (0.75, 0.75, 0.75), respectively. The D-site usually contains an *s*- or *p*-element, while A-, B-, and C-sites usually contain *d*-elements.

In the case of the $L2_1$ structure (Figure 1a), all X atoms are equivalent and occupy the A- and C-sites. The Y and Z atoms occupy the B- and D-sites, respectively. The first coordination sphere of X atoms includes four Y and four Z atoms, while the second one consists of six X atoms. Y atoms have eight X atoms as nearest neighboring positions, and the next-nearest neighbors are six Z atoms. In turn, Z atoms are surrounded by eight X atoms in the first coordination sphere and six Y atoms in the second coordination sphere.

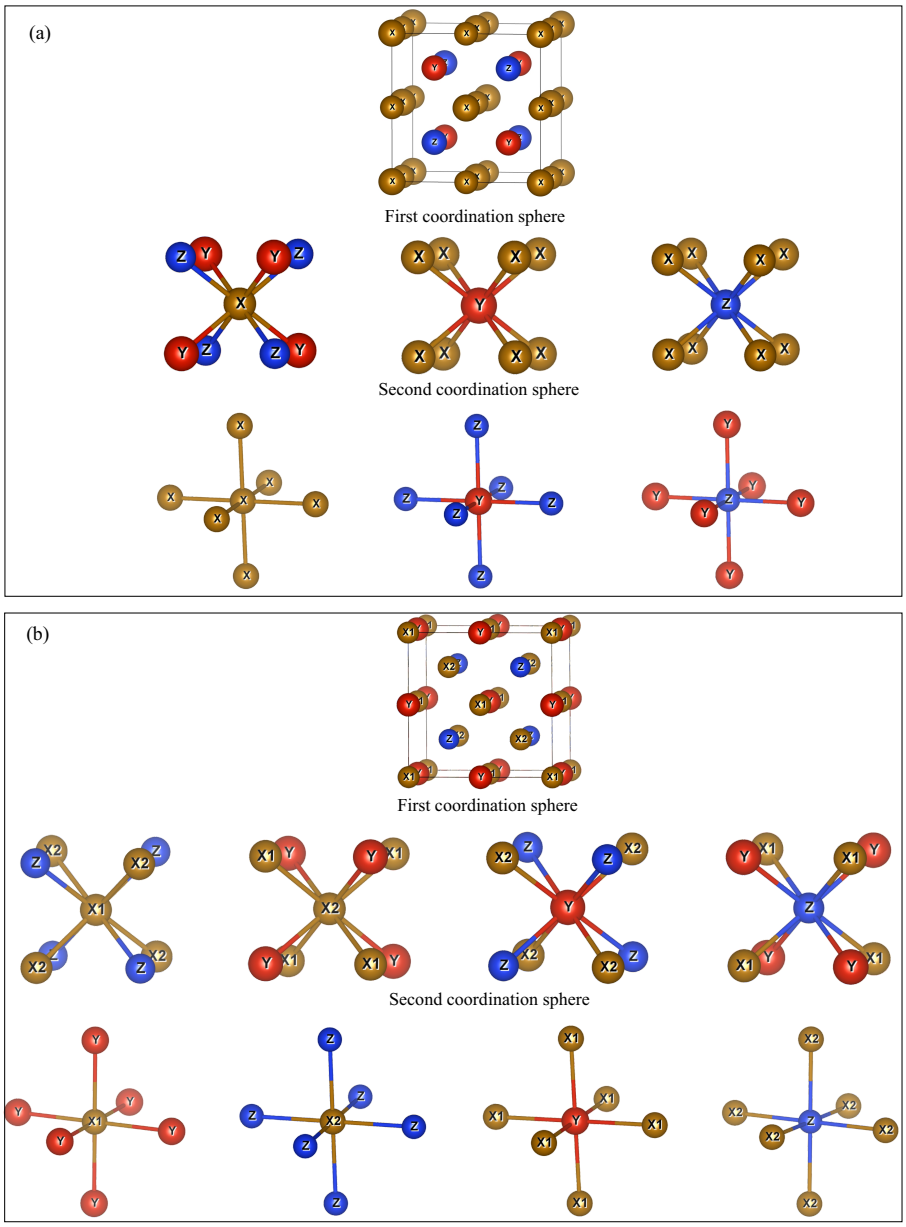

Figure 1. Crystal structure and nearest and next-nearest local environment of Heusler compounds in (**a**) $L2_1$ and (**b**) XA structures.

In the XA structure, there is a permutation of X atoms in the C-site and Y atoms in the B-site. In this case, the structure is characterized by two symmetrically non-equivalent X atoms, which are designated as X1 and X2, respectively. These atoms differ in their local

environment. In the first coordination sphere, X1 atoms are surrounded by metal and non-metal atoms (four X2 and four Z atoms), while X2 atoms are surrounded only by metal atoms (four X1 and four Y atoms). This difference in the local environment determines the difference in the physical properties of X1 and X2 atoms. Y atoms have four Z and four X2 atoms in the first coordination sphere and six X1 atoms in the second coordination sphere. Z atoms have four X1 and four Y atoms as nearest neighbors, and six X2 atoms as next-nearest neighbors.

3.1. Structure Stability

The results of the formation enthalpy calculations are given in Table 1. The calculated formation enthalpies of all compounds are negative, which indicates their stability with respect to decomposition into the isochemical mixture 2M1 + M2 + Si (M1 = V, Fe; M2 = Fe, V) and the possibility of their formation in the experiment. In the case of V_2FeSi, the energetically more favorable phase is XA, while for Fe_2VSi, the energetically more favorable phase is $L2_1$. The result obtained is consistent with the available experimental data, where it is reported that Fe_2VSi is realized in the $L2_1$ structure [6]. It should be noted that there are no such experimental data for V_2FeSi.

Table 1. Calculated formation enthalpies and energy differences between $L2_1$ and XA structures of V_2FeSi and Fe_2VSi.

Compounds	ΔH(eV/f.u.)		Stable Structure
	$L2_1$	XA	
V_2FeSi	−1.118	−1.420	XA
Fe_2VSi	−1.632	−1.256	$L2_1$

The equilibrium lattice parameters and magnetic moments of V_2FeSi and Fe_2VSi for both $L2_1$ and XA structures are given in Table 2. The lattice constants Fe_2VSi-$L2_1$ calculated using the SCAN functional are about 2% smaller than the previous theoretical (GGA) and experimental results [6,21]. This is because the simulation was carried out at zero temperature, while the experimentally measured value was obtained at room temperature. Accounting for thermal expansion within SCAN calculations should give a more accurate agreement with the experimental data. It should be noted that in GGA-based calculations [21], the volume of the structure was not relaxed and fixed to the experimental one from ref [6].

Table 2. Calculated lattice parameters (Å) and magnetic moments (μ_B) of V_2FeSi and Fe_2VSi in regular and inverse structures in comparison with available theoretical and experimental data.

Comp.	Str.	Method	Lattice Param.		A-Site Atom		B-Site Atom		C-Site Atom		D-Site Atom		Total
V_2FeSi	XA	SCAN	5.748	[this work]	V1	1.730	V2	−0.707	Fe	1.070	Si	−0.056	2.00
	$L2_1$	SCAN	5.805	[this work]	V	1.541	Fe	1.170	V	1.541	Si	0.025	4.02
	$L2_1$	GGA	5.80	Ref. [18]	V	−1.55	Fe	−0.930	V	−1.55	Si	0.05	−1.99
Fe_2VSi	XA	SCAN	5.727	[this work]	Fe1	1.765	Fe2	2.646	V	−1.869	Si	0.007	2.48
	$L2_1$	SCAN	5.556	[this work]	Fe	0.629	V	−0.255	Fe	0.622	Si	−0.024	0.92
	$L2_1$	GGA	5.670	Ref. [21]	Fe	0.59	V	−0.10	Fe	0.59	Si	−0.01	0.99
	$L2_1$	exp.	5.675	Ref. [20]	Fe	0.22			Fe	0.22			
	$L2_1$	exp.	–	Ref. [39]	Fe	0.9			Fe	0.9			
	$L2_1$	exp.	5.670	Ref. [6]									

3.2. Electronic Structure: Density of States

In Figure 2, the total electron densities of states (TDOS) of V_2FeSi and Fe_2VSi compounds in $L2_1$ and XA structures are shown. V_2FeSi and Fe_2VSi, in their energetically favorable structures XA (Figure 2a) and $L2_1$ (Figure 2d), respectively, reveal electronic

properties close to half-metallic. There are pseudogaps in TDOS for α-states V_2FeSi-XA and β-states for Fe_2VSi-$L2_1$. All the metastable structures are metallic.

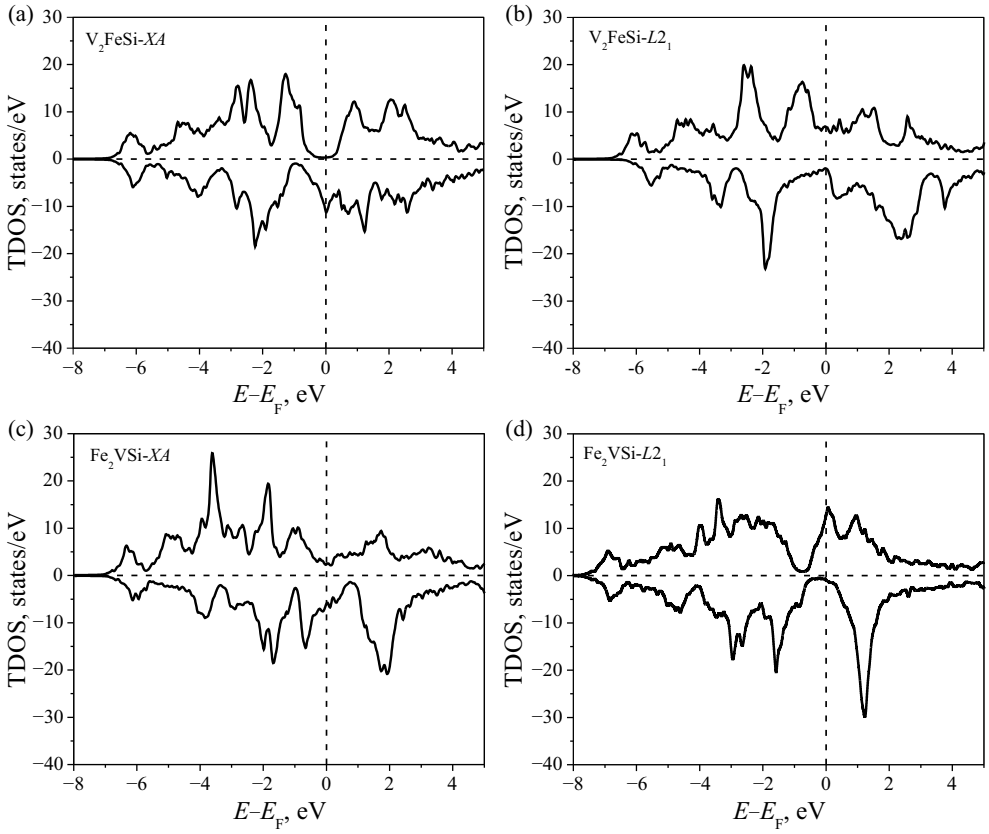

Figure 2. Calculated total density of states for V_2FeSi in (**a**) XA and (**b**) $L2_1$ structures, and for Fe_2VSi in (**c**) XA and (**d**) $L2_1$ structures.

The projected densities of states (PDOS) for the investigated structures are presented in Figures 3 and 4. In all cases considered, the contribution of the Si-p states is much smaller than the contributions of the d-states of transition metals and becomes significant at energies below -3 eV (here and below, the energy levels are counted from the E_F Fermi level).

For the metastable V_2FeSi-$L2_1$ (Figure 3), there is an energy gap near the Fermi level for the d-states of Fe atoms. In this case, the electronic structure typical for metals is formed due to the $e_g(\alpha)$ and $t_{2g}(\beta)$ states on V atoms. In the case of the V_2FeSi-XA structure, the bandgap occurs for the spin-majority states. The metallic properties of β-states are due to the e_g electrons of vanadium atoms.

For the compound Fe_2VSi (Figure 4), in the case of an energetically favorable $L2_1$ lattice, the metallic properties of α-states are provided by the t_{2g} electrons of Fe atoms. The $t_{2g}(\beta)$-states of V atoms create a pseudogap with a relatively poor density of states. The metallic properties of the Fe_2VSi-XA metastable structure are created by the e_g states on Fe atoms and $e_g(\beta)$ electrons on V atoms.

The location of Fe and V atoms in the structure plays a substantial role in the appearance of half-metallic properties in the considered Heusler alloys. From the obtained results, it can be seen that the bonds that arise between the neighboring metal atoms are responsible for the appearance of a half-metallic pseudogap. Since the nearest metal–metal neighbors are located along the (111) direction in the structure, the formation of bonds is mainly associated with the overlapping of the t_{2g} orbitals of Fe and V atoms. It should also be noted that a half-metallic pseudogap appears only when the B-site is occupied by a V atom with a relatively small magnetic moment. If the B-site is occupied by an Fe atom with a relatively large magnetic moment, then the energy gap disappears and the alloy becomes metal.

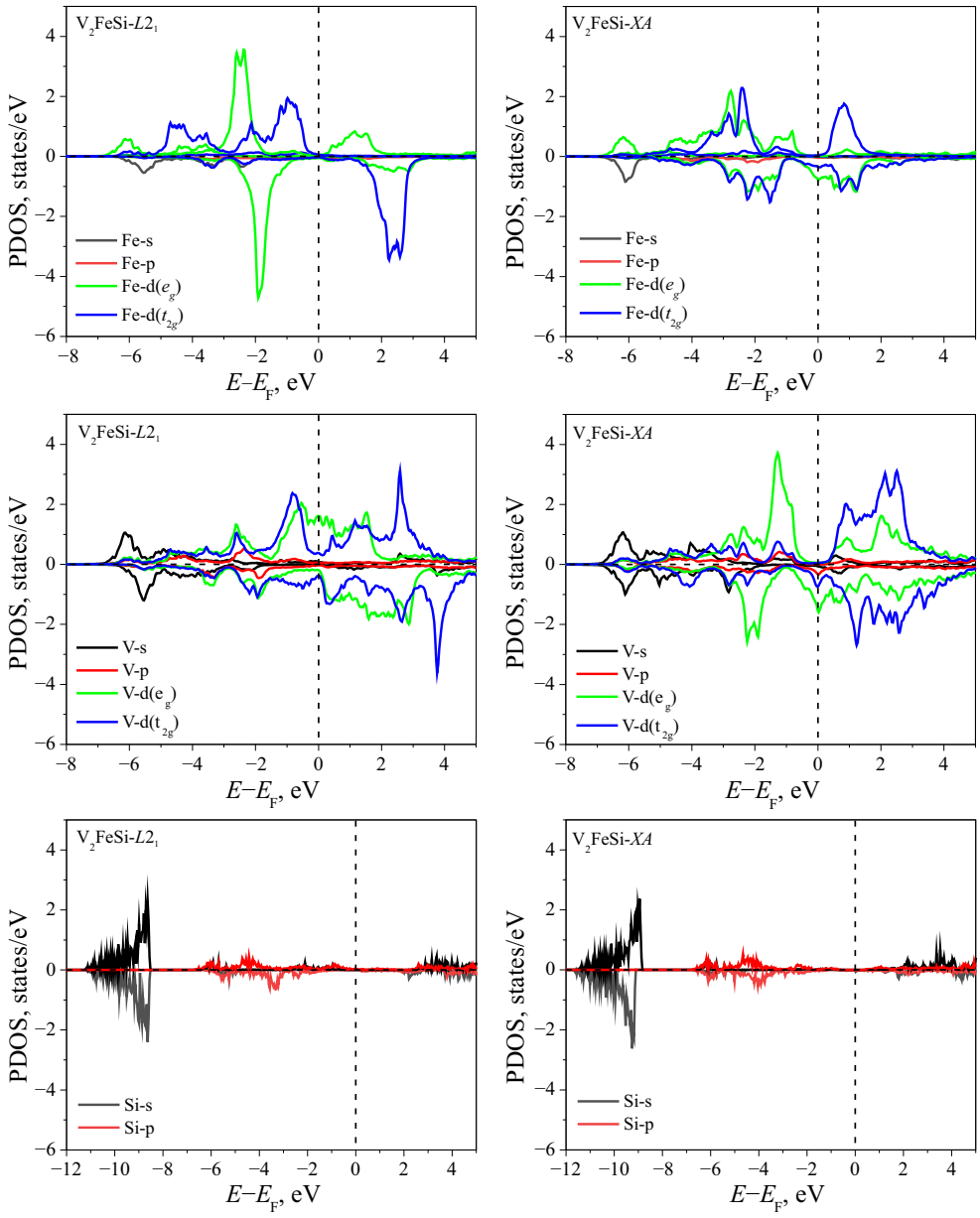

Figure 3. The partial density of states for V_2FeSi of both $L2_1$ and XA structures. Zero on the energy axis corresponds to the Fermi level.

The absence of conduction electrons near the Fermi level, or the formation of a bandgap, for a particular spin projection indicates that these electrons are localized and participate in the formation of covalent bonds. In contrast, the presence of an electron density near E_F indicates the metallic nature of the bond in this compound. The covalent bond is more vital than the metallic one, which should result in stabilizing the respective structures compared to structures with a metallic bond. This effect can be quantified using the COHP analysis, which has also been carried out and presented in the following.

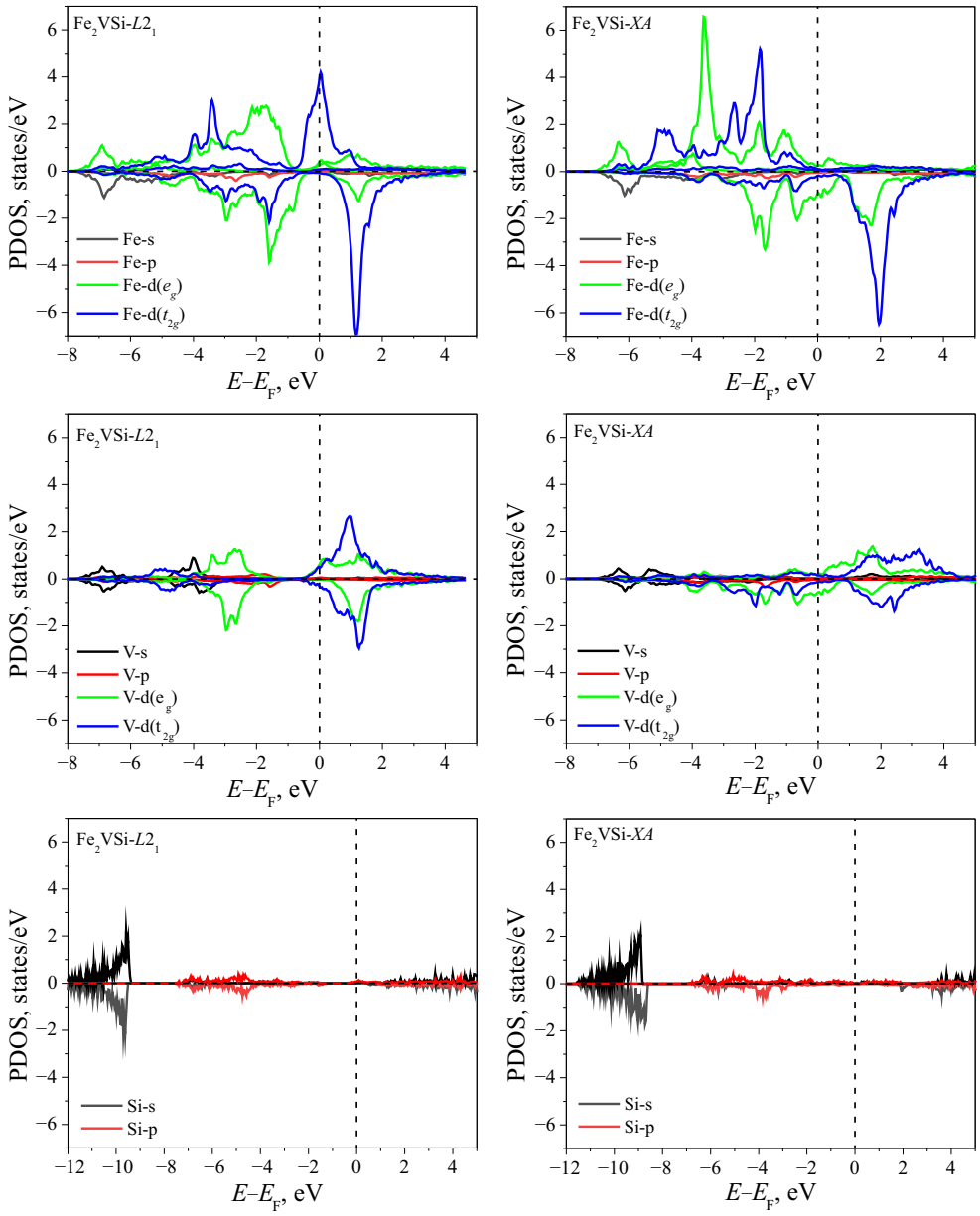

Figure 4. The partial density of states for Fe_2VSi of both $L2_1$ and XA structures. Zero on the energy axis corresponds to the Fermi level.

3.3. Electronic Structure: Chemical Bonding

The results of the COHP analysis for interactions between atoms of the first and second coordination spheres are shown in Figures 5 and 6. For Fe_2VSi, the interatomic bonds from −1 eV to the Fermi level are antibonding except for the Si–V interaction. −COHP for β-states near the Fermi level are close to zero (Figure 5a,b), which corresponds to the non-bonding nature of the bond. The stability of the system is ensured by the electronic bonds of the nearest neighbors Si–Fe and V–Fe, which formed electronic states with energies below −3 eV and −2.5 eV (here and below, all energies are considered relative to the Fermi level) (Figure 5a). In addition, the interactions between atoms in the second Si–V coordination sphere at energies below −4 eV make a significant contribution (Figure 5b). This nature of interatomic bonds, in which α-states (except Si–V in the second coordination sphere) are anti-bonding and β-states are non-bonding, explains the metallic behavior of the α-electrons and reduced DOS for the β-electrons.

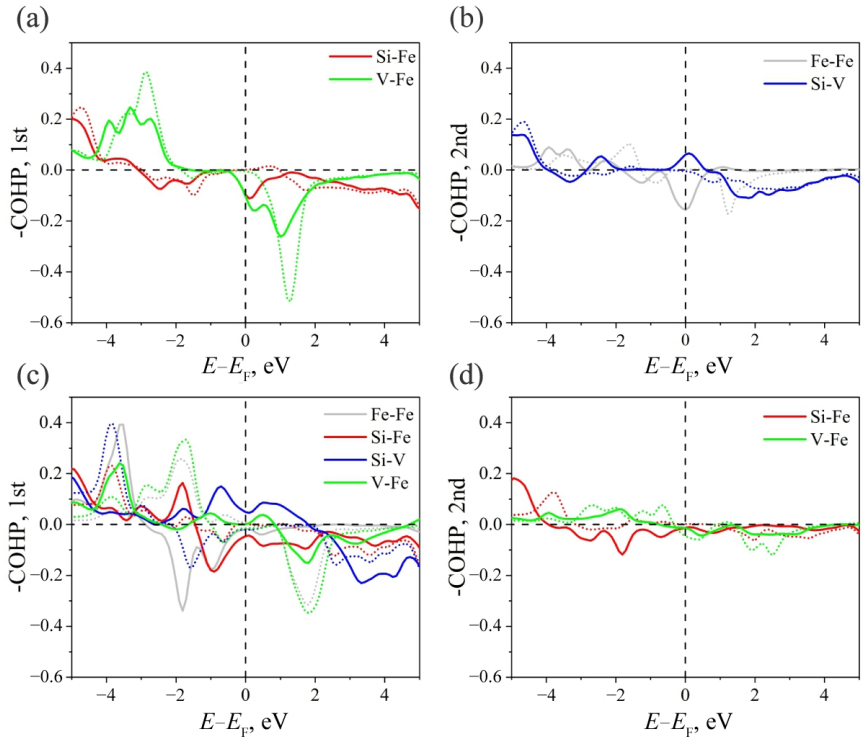

Figure 5. −COHP for (**a**) the first and (**b**) the second coordination spheres of atoms in the Fe_2VSi Heusler alloy of structure $L2_1$. −COHP for (**c**) the first and (**d**) second coordination spheres of atoms in the Fe_2VSi Heusler alloy of the XA structure.

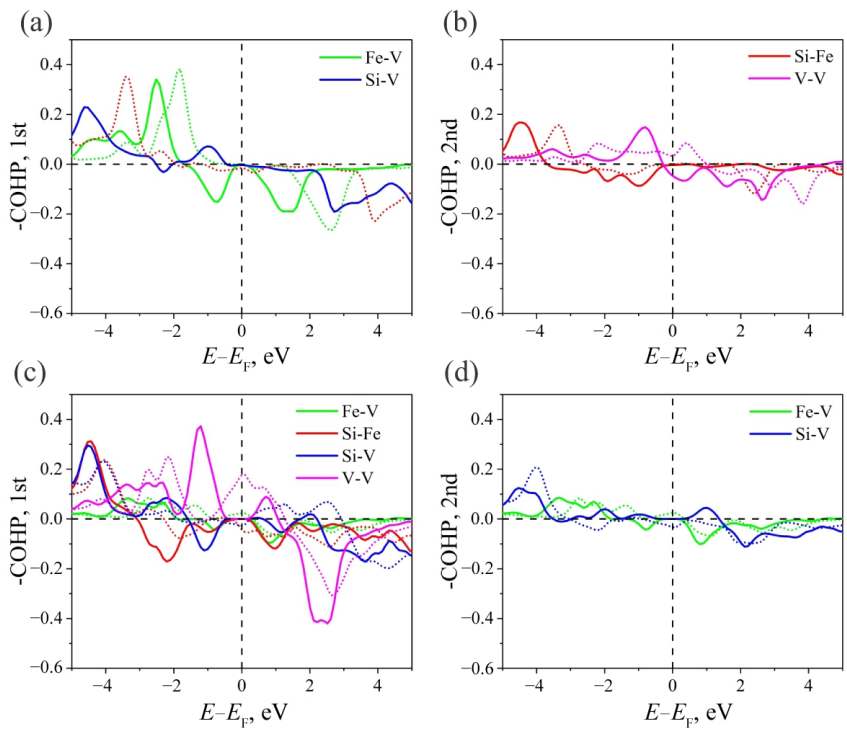

Figure 6. −COHP for (**a**) the first and (**b**) the second coordination spheres of atoms in the V_2FeSi Heusler alloy of the $L2_1$ structure. −COHP for (**c**) the first and (**d**) second coordination spheres of atoms in the V_2FeSi Heusler alloy of the XA structure.

In the Fe_2VSi-XA system near E_F, all interactions between atoms in the first coordination sphere are anti-bonding or nearly non-bonding (Figure 5c,d). The exception is Si–V

(α-states), which has a bonding character. The interaction between atoms in the second coordination sphere near the Fermi level is close to non-bonding, except for the interaction of V–Fe (β-states), which are anti-bonding. At lower energies, the V–Fe bond for both spin projections has a weak bonding character. The Si–Fe (α-states) bond is anti-bonding down to energies of −4 eV, while the Si–Fe (β-states) bond is non-bonding down to −3 eV. This character of chemical bonds, which is mainly non-bonding and anti-bonding for both spin projections near E_F, explains the metallic properties of the Fe_2VSi-XA structure.

A similar analysis can be carried out in the case of V_2FeSi compounds (Figure 6a,b). V_2FeSi-$L2_1$ is characterized by a non-bonding character of chemical bonding between the atoms of the first coordination sphere with a weak anti-bonding interaction of the β-states of the Si–V bond near E_F. In the second coordination sphere, near the Fermi level, the Si–Fe bond has a non-bonding character for both spin projections. The presence of anti-bonding interactions for both spin projections provides the metallic character of V_2FeSi-$L2_1$. As in the cases considered above, the stability of the structure is ensured by the interaction between deep-lying states.

V_2FeSi-XA is characterized by a non-bonding character of chemical bonding near the Fermi level for all α-states for both considered coordination spheres (Figure 6c,d). In the first coordination sphere, V–V (β-states) bonds have a pronounced bonding character, while Si–V (β-states) and Si–Fe (β-states) are anti-bonding. In the second coordination sphere, Fe–V (β-states) and Si–V (β-states) bonds have a bonding and anti-bonding character, correspondingly. The presence of anti-bonding α-states does not make the system conductive for these states, since α-PDOS(V) near the Fermi level is zero, which explains the presence of a bandgap for α-states (Figure 3). The presence of anti-bonding states and non-zero PDOS for β-states for d-electrons near E_F provides the metallic properties of the system for electrons of a given spin direction.

The integrated −COHP values to E_F (−ICOHPs) are presented in Table 3. Here, we have considered the values for the first three coordinate spheres of each atom. The maximum contribution of the third coordination sphere to the total value of −COHP ($\sum$) is 2.6 % (V_2FeSi-XA). For this reason, the contribution of the interaction of atoms in this coordination sphere is not considered in detail. Since the distances between atoms and their environment in the fourth coordination sphere are 4.8–5 Å, we neglect the contribution of these interactions.

The value $\sum$ for the Fe_2VSi-$L2_1$ structure is greater than the corresponding value for Fe_2VSi-XA. This fact means that the chemical bonds in Fe_2VSi-$L2_1$ are more substantial than in Fe_2VSi-XA, which explains the lower values of the ground-state energy and the formation enthalpy of Fe_2VSi-$L2_1$ (Table 1). For V_2FeSi, the ratio of $\sum$ of the $L2_1$ and XA structures is opposite; i.e., chemical bonds in V_2FeSi-$L2_1$ are weaker than in V_2FeSi-XA. The relations obtained between the values of $\sum$ explain why the $L2_1$ and XA structures are more favorable for the Fe_2VSi and V_2FeSi, respectively.

The total −ICOHP for the interaction of atoms of the first coordination sphere is approximately two times greater than the corresponding value for the second coordination sphere. The most considerable dependence on the spin direction is observed for pairs of Fe–Fe atoms. For these pairs of atoms, the −ICOHP values of α-states are 2 ($L2_1$, second shell) and 3 (XA, first shell) times smaller than the corresponding values for β-states. In all considered Fe_2VSi and V_2FeSi lattices, the d electrons of the Fe and V atoms are strongly coupled to the p electrons of Si. In both Fe_2VSi modifications, the Fe1–Fe2 (XA) and Fe–Fe ($L2_1$) bonds are almost two times weaker than the analogous V1–V2 (XA) and V–V ($L2_1$) bonds in the V_2FeSi system. −ICOHP for V–Fe bonds between nearest neighbors is approximately the same for all considered structures. The Fe–V interaction between the atoms in the second coordination sphere is more vital in the V_2FeSi-XA compared to the same value in Fe_2VSi-XA. It should be noted that in the Fe_2VSi system, the average values of −ICOHP in the $L2_1$ structure are more significant than the corresponding values in the XA structure for all three coordination spheres considered. In the case of V_2FeSi, the XA

structure is stabilized due to the contribution of the interaction of atoms in the second coordination sphere.

Table 3. Calculated −ICOHP values for all types of atomic pairs in the first and second coordination spheres. The average values of all interatomic interactions are given for the third coordination sphere. *R* stands for interatomic distances. The data are given for different spin projections—α and β states. The total corresponds to the sum of α and β values of −ICOHP, while $\sum$ means the sum of average −ICOHP values for all three coordination spheres.

Fe_2VSi *$L2_1$*						**V_2FeSi** *$L2_1$*					
Shell	**Bond**	***R* (Å)**	**−ICOHP (eV/bond)**			**Shell**	**Bond**	***R* (Å)**	**−ICOHP (eV/bond)**		
			β	**α**	**Total**				**β**	**α**	**Total**
1	Fe–V	2.406	0.593	0.546	1.139	1	Fe–V	2.514	0.499	0.413	0.912
	Fe–Si	2.406	0.714	0.7	1.414		V–Si	2.514	0.845	0.825	1.67
	Average	2.406	0.653	0.623	1.276		Average	2.514	0.672	0.619	1.291
2	V–Si	2.778	0.46	0.473	0.933	2	Fe–Si	2.903	0.294	0.212	0.506
	Fe–Fe	2.778	0.19	0.108	0.298		V–V	2.903	0.255	0.306	0.561
	Average	2.778	0.325	0.29	0.615		Average	2.903	0.275	0.259	0.534
3	Average	3.929	0.023	0.022	0.045	3	Average	4.105	0.013	0.02	0.033
$\sum$					1.936	$\sum$					1.858
Fe_2VSi *XA*						**V_2FeSi** *XA*					
Shell	**Bond**	***R* (Å)**	**−ICOHP (eV/bond)**			**Shell**	**Bond**	***R* (Å)**	**−ICOHP (eV/bond)**		
			β	**α**	**Total**				**β**	**α**	**Total**
1	Fe1–Si	2.48	0.669	0.68	1.349	1	Fe–Si	2.489	0.719	0.592	1.311
	V–Si	2.48	0.83	0.86	1.69		V2–Si	2.489	0.795	0.821	1.616
	Fe1–Fe2	2.48	0.471	0.164	0.635		V1–V2	2.489	0.542	0.672	1.214
	Fe2–V	2.48	0.564	0.404	0.968		Fe–V1	2.489	0.572	0.425	0.997
	Average	2.48	0.635	0.526	1.161		Average	2.489	0.657	0.627	1.284
2	Fe1–Si	2.864	0.321	0.217	0.538	2	V1–Si	2.874	0.399	0.188	0.587
	V–Fe2	2.864	0.243	0.201	0.444		V2–Fe	2.874	0.222	0.408	0.63
	Average	2.864	0.282	0.209	0.491		Average	2.874	0.311	0.298	0.609
3	Average	4.05	0.022	0.017	0.039	3	Average	4.065	0.016	0.035	0.051
$\sum$					1.691	$\sum$					1.944

3.4. Magnetic Properties

The value of the magnetic moments of individual transition metal atoms depends on the local environment. It could be assumed that the magnetic moment of the *d*-element atom will decrease with an increase in the concentration of Z atoms in its nearest neighboring positions. For example, it was stated in ref [26,40] that in ordered Fe_xSi_{1-x} alloys, an increase in the concentration of Si in the first coordination sphere of Fe leads to a decrease in the magnetic moment. However, this statement is not entirely true, since the main effect on the change in the magnetic moment of the atom is still exerted by the next-nearest neighbors located in the second coordination sphere [41]. The presence of *d*-elements at the nearest neighboring positions leads to the formation of strong σ-bonds between the *d*-electrons of these atoms. In this case, the delocalization of *d*-electrons and a decrease in the magnetic moment are observed [41,42].

The results of magnetic moment calculations for all structures considered are summarized in Table 2. To determine the preferred magnetic configuration for each structure, in addition to initial ferromagnetic configuration, we have performed the calculations with initial antiferromagnetic configurations. As reported in ref [43], we have considered one initial antiferromagnetic configuration for $L2_1$ structures and three possible antiferromagnetic configurations for *XA* structures (Figure 7). Regardless of the choice of the initial

magnetic configuration, the relaxation of Fe_2VSi-XA, Fe_2VSi-$L2_1$, and V_2FeSi-XA lead to ferrimagnetic ordering, while the relaxation of V_2FeSi-$L2_1$ lead to ferromagnetic ordering.

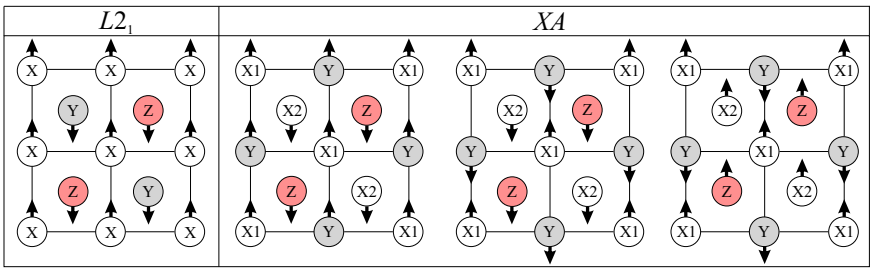

Figure 7. The types of initial antiferromagnetic configurations for $L2_1$ and XA structures.

According to available experimental data, Fe_2VSi is an antiferromagnet, while our calculations showed that it should be a ferrimagnet. Such inconsistency between experiments and calculations may be due to the fact that antiferromagnetism in Fe_2VSi is found to strongly depend on the degree of atomic disorder, as was stated by Nishihara et al. [39]. Such a theory–experiment discrepancy is also reported for Mn_2FeSi [43,44] and Mn_3Si [45].

In the case of V_2FeSi, the values of the total magnetic moments of the XA structure (2.0 μ_B/f.u.) obtained using the SCAN functional completely obey the Slater–Pauling (S-P) rule up to the orientation of the magnetic moments. According to this rule, the total magnetic moment in Heusler alloys can be found by the formula $M_t = Z_t - 24$, where Z_t is the total number of valence electrons per unit cell, and M_t – the magnetic moment per formula unit. The $L2_1$ structure (4.02 μ_B/f.u.) does not satisfy this rule due to the ferromagnetic bonding of the V and Fe atoms. For Fe_2VSi, the value of the total magnetic moment of the $L2_1$ structure (0.92 μ_B) is close to the S-P rule prediction of 1.0 μ_B/f.u. For the XA type, the value of the total magnetic moment, equal to 2.48 μ_B, is significantly different from the S-P rule obtained value (Table 2). In all the cases considered, the magnitudes of atomic magnetic moments of transition-metal atoms are smaller for stable structures of the corresponding stoichiometry except for V atoms at the A sites of the V_2FeSi compound.

An analysis of the −ICOHP values also makes it possible to explain the dependence of the magnetic moment on the transition-metal atoms in the considered compounds. The results obtained correspond to the fact that the weaker the interaction of atoms in the environment, the greater the magnitude of the magnetic moment on them.

In the case of Fe atoms, their magnetic moment corresponds to α states. For this reason, we consider the −ICOHP values for α-states. The −ICOHP(α) values averaged over the first and second coordination spheres of Fe atoms in Fe_2VSi compounds are the 0.402 eV/bond for the $L2_1$ structure and the 0.334 eV/bond (Fe1) and 0.248 eV/bond (Fe2) for the XA structure. For V_2FeSi, the corresponding −ICOHP values are 0.292 ($L2_1$) and 0.465 (XA). As the values of −ICOHP decrease, the value of the magnetic moment on the Fe atoms increases (Table 2).

A similar analysis in the case of V atoms gives the same dependence of the magnitude of the magnetic moment on the atom on the value of −ICOHP (taking into account the direction of the spin). The −ICOHP values averaged over the first and second coordination spheres of V atoms in V_2FeSi compounds are 0.485 eV/bond for the $L2_1$ structure and 0.394 eV/bond (V1), and 0.477 eV/bond (V2) for the XA structure. For Fe_2VSi, the corresponding –ICOHP values are 0.536 ($L2_1$) and 0.502 (XA).

Thus, there is a direct correlation between the value of −ICOHP on a transition metal atom and the value of its magnetic moment. The smaller −ICOHP, the larger the value of μ. It should be noted that in the case of V_2FeSi-XA, in contrast to Fe_2VSi-$L2_1$, the interaction of α states is more vital. For this reason, the bandgap appears in it for α states, although the total magnetic moment is directed upwards.

4. Conclusions

We have employed the DFT method with SCAN to investigate the electronic and magnetic properties of Fe_2VSi and V_2FeSi alloys. It is concluded that Fe_2VSi is stable in regular structure, while V_2FeSi is stable in inverse structure. Both alloys are ferrimagnets and reveal electronic properties close to half-metallic with pseudogaps in β-states for Fe_2VSi-$L2_1$ and α-states for V_2FeSi-XA. In addition, structural stability, electronic and magnetic properties of considered Heusler alloys have been explained in terms of chemical bonding within the COHP formalism.

Author Contributions: Conceptualization, T.I. and V.K.; methodology, T.I.; validation, T.I. and N.S.; formal analysis, N.M. and A.A.; investigation, N.M. and A.A.; writing—original draft preparation, A.A., N.M., N.S., and T.I.; writing—review and editing, F.A. and V.K.; visualization, N.M.; supervision, T.I. and V.K.; funding acquisition, T.I. All authors have read and agreed to the published version of the manuscript.

Funding: This work was performed under the grant project AP08855879 "First-principles design of effective magnetostriction materials for practical applications" for 2020–2022 by the Ministry of Education and Science of the Republic of Kazakhstan. One of the authors (VVK) acknowledges the Russian Science Foundation (grant No. 21-42-00035).

Data Availability Statement: Not applicable.

Acknowledgments: The calculations were performed at the supercomputer cluster provided by the Materials Modeling and Development Laboratory at NUST "MISIS". The authors are grateful to the Supercomputer Center, Novosibirsk State University, for access to the resources of the cluster.

Conflicts of Interest: The authors declare no conflict of interest.

References

1. Bakkar, S.A. *New Inverse-Heusler Materials with Potential Spintronics Applications*; Southern Illinois University at Carbondale: Carbondale, IL, USA, 2017.
2. Granovskii, A.; Soboleva, E.; Fadeev, E.; Dubenko, I.; Aryal, A.; Samassekou, H.; Pandey, S.; Stadler, S.; Mazumdar, D.; Ali, N.; et al. Martensitic Phase Transition in Magnetic Thin Films Based on Inverse Mn_2FeSi Heusler Alloys. *J. Exp. Theor. Phys.* **2020**, *130*, 117–122. [CrossRef]
3. Miki, H.; Ohoyama, K.; Funahashi, S.; Tomiyoshi, S.; Yamaguchi, Y. Crystallographic and magnetic structure of the itinerant-electron antiferromagnets $Mn_{3-x}T_xSi$ (T = Cr, Fe). *Phys. B Condens. Matter* **1995**, *213*, 360–362. [CrossRef]
4. Nishino, Y.; Inoue, S.Y.; Asano, S.; Kawamiya, N. Anomalous temperature dependence of the electrical resistivity in binary and pseudobinary alloys based on Fe_3Si. *Phys. Rev. B* **1993**, *48*, 13607. [CrossRef] [PubMed]
5. Endo, K.; Tokiyama, M.; Matsuda, H.; Ooiwa, K.; Goto, T.; Arai, J. Anomalous Transport and Magnetic Properties in $Fe_{2+x}V_{1-x}Si$ in Relation to the Origin of GMR. *J. Phys. Soc. Jpn.* **2004**, *73*, 1944–1952. [CrossRef]
6. Ito, M.; Kai, K.; Furuta, T.; Manaka, H.; Terada, N.; Hiroi, M.; Kondo, A.; Kindo, K. Thermodynamic properties of Heusler Fe_2VSi. *AIP Adv.* **2018**, *8*, 055703. [CrossRef]
7. Nagano, T.; Uwanuyu, S.; Kawakami, M. Magnetic properties of the Fe_2MnSi- and Fe_2VSi-based Heusler alloys. *J. Magn. Magn. Mater.* **1995**, *140*, 123–124. [CrossRef]
8. Cui, Y.; Kimura, A.; Miyamoto, K.; Sakamoto, K.; Xie, T.; Qiao, S.; Nakatake, M.; Shimada, K.; Taniguchi, M.; Fujimori, S.I.; et al. Electronic structures of $Fe_{3-x}V_xSi$ probed by photoemission spectroscopy. *Phys. Status Solidi (A)* **2006**, *203*, 2765–2768. [CrossRef]
9. Nishino, Y.; Kato, M.; Asano, S.; Soda, K.; Hayasaki, M.; Mizutani, U. Semiconductorlike behavior of electrical resistivity in Heusler-type Fe_2VAl compound. *Phys. Rev. Lett.* **1997**, *79*, 1909. [CrossRef]
10. Ullakko, K.; Huang, J.K.; Kantner, C.; O'Handley, R.C.; Kokorin, V.V. Large magnetic-field-induced strains in Ni_2MnGa single crystals. *Appl. Phys. Lett.* **1996**, *69*, 1966–1968. [CrossRef]
11. Ullakko, K.; Huang, J.; Kokorin, V.; O'Handley, R. Magnetically controlled shape memory effect in Ni_2MnGa intermetallics. *Scr. Mater.* **1997**, *36*, 1133–1138. [CrossRef]
12. Rasul, M.N.; Javed, A.; Khan, M.A.; Hussain, A. Structural stability, mechanical, electronic and magnetic behaviour of quaternary ScNiCrX (X = Al, Ga) Heusler alloys under pressure. *Mater. Chem. Phys.* **2019**, *222*, 321–332. [CrossRef]
13. Abada, A.; Amara, K.; Hiadsi, S.; Amrani, B. First principles study of a new half-metallic ferrimagnets Mn_2-based full Heusler compounds: Mn_2ZrSi and Mn_2ZrGe. *J. Magn. Magn. Mater.* **2015**, *388*, 59–67. [CrossRef]
14. Ze-Jin, Y.; Qing-He, G.; Heng-Na, X.; Ju-Xiang, S.; Xian-Wei, W.; Zhi-Jun, X. Pressure-induced magnetic moment abnormal increase in Mn_2FeAl and non-continuing decrease in Fe_2MnAl via first principles. *Sci. Rep.* **2017**, *7*, 16522. [CrossRef]
15. Qi, S.; Zhang, C.H.; Chen, B.; Shen, J.; Chen, N. First-principles study on the ferrimagnetic half-metallic Mn_2FeAs alloy. *J. Solid State Chem.* **2015**, *225*, 8–12. [CrossRef]

16. Khandy, S.A.; Chai, J.D. Novel half-metallic $L2_1$ structured full-Heusler compound for promising spintronic applications: A DFT-based computer simulation. *J. Magn. Magn. Mater.* **2019**, *487*, 165289. [CrossRef]
17. Abuova, F.; Inerbaev, T.; Abuova, A.; Merali, N.; Soltanbek, N.; Kaptagay, G.; Seredina, M.; Khovaylo, V. Structural, Electronic and Magnetic Properties of $Mn_2Co_{1-x}V_xZ$ (Z = Ga, Al) Heusler Alloys: An Insight from DFT Study. *Magnetochemistry* **2021**, *7*, 159. [CrossRef]
18. Skaftouros, S.; Özdoğan, K.; Şaşıoğlu, E.; Galanakis, I. Generalized Slater-Pauling rule for the inverse Heusler compounds. *Phys. Rev. B* **2013**, *87*, 024420. [CrossRef]
19. Lue, C.S.; Ross, J.H., Jr.; Chang, C.; Yang, H. Field-dependent specific heat in Fe_2VAl and the question of possible 3d Heavy Fermion behavior. *Phys. Rev. B* **1999**, *60*, R13941. [CrossRef]
20. Endo, K.; Matsuda, H.; Ooiwa, K.; Itoh, K. Antiferromagnetism in a Heusler alloy Fe_2VSi. *J. Phys. Soc. Jpn.* **1995**, *64*, 2329–2332. [CrossRef]
21. Joshi, P.K.; Kumar, K.; Arora, G.; Mali, D.; Jangid, P.K.; Ahuja, B.L. First-principles investigations of electronic and magnetic properties of $Fe_2V_{1-x}Cr_xSi$ Heusler alloys. *J. Phys. Conf. Ser.* **2021**, *1849*, 012030. [CrossRef]
22. Fujii, S.; Ishida, S.; Asano, S. Antiferromagnetism and atomic disorder in Fe_2VSi. *J. Phys. Soc. Jpn.* **2004**, *73*, 459–463. [CrossRef]
23. Hirohata, A.; Yamada, K.; Nakatani, Y.; Prejbeanu, I.L.; Dieny, B.; Pirro, P.; Hillebrands, B. Review on spintronics: Principles and device applications. *J. Magn. Magn. Mater.* **2020**, *509*, 166711. [CrossRef]
24. Elphick, K.; Frost, W.; Samiepour, M.; Kubota, T.; Takanashi, K.; Sukegawa, H.; Mitani, S.; Hirohata, A. Heusler alloys for spintronic devices: Review on recent development and future perspectives. *Sci. Technol. Adv. Mater.* **2021**, *22*, 235–271. [CrossRef]
25. Kim, S.K.; Beach, G.S.D.; Lee, K.J.; Ono, T.; Rasing, T.; Yang, H. Ferrimagnetic spintronics. *Nat. Mater.* **2022**, *21*, 24–34. [CrossRef] [PubMed]
26. Niculescu, V.; Burch, T.; Budnick, J. A local environment description of hyperfine fields and atomic moments in $Fe_{3-x}T_xSi$ alloys. *J. Magn. Magn. Mater.* **1983**, *39*, 223–267. [CrossRef]
27. Kresse, G.; Furthmüller, J. Efficiency of ab-initio total energy calculations for metals and semiconductors using a plane-wave basis set. *Comput. Mater. Sci.* **1996**, *6*, 15–50. [CrossRef]
28. Kresse, G.; Furthmüller, J. Efficient iterative schemes for ab initio total-energy calculations using a plane-wave basis set. *Phys. Rev. B* **1996**, *54*, 11169. [CrossRef]
29. Kresse, G.; Joubert, D. From ultrasoft pseudopotentials to the projector augmented-wave method. *Phys. Rev. B* **1999**, *59*, 1758. [CrossRef]
30. Blöchl, P.E. Projector augmented-wave method. *Phys. Rev. B* **1994**, *50*, 17953. [CrossRef]
31. Sun, J.; Remsing, R.C.; Zhang, Y.; Sun, Z.; Ruzsinszky, A.; Peng, H.; Yang, Z.; Paul, A.; Waghmare, U.; Wu, X.; et al. Accurate first-principles structures and energies of diversely bonded systems from an efficient density functional. *Nat. Chem.* **2016**, *8*, 831–836. [CrossRef]
32. Monkhorst, H.J.; Pack, J.D. Special points for Brillouin-zone integrations. *Phys. Rev. B* **1976**, *13*, 5188. [CrossRef]
33. Zhang, Y.; Kitchaev, D.A.; Yang, J.; Chen, T.; Dacek, S.T.; Sarmiento-Perez, R.A.; Marques, M.A.L.; Peng, H.; Ceder, G.; Perdew, J.P.; et al. Efficient first-principles prediction of solid stability: Towards chemical accuracy. *Npj Comput. Mater.* **2018**, *4*, 9. [CrossRef]
34. Deringer, V.L.; Tchougréeff, A.L.; Dronskowski, R. Crystal orbital Hamilton population (COHP) analysis as projected from plane-wave basis sets. *J. Phys. Chem. A* **2011**, *115*, 5461–5466. [CrossRef] [PubMed]
35. Dronskowski, R.; Bloechl, P.E. Crystal orbital Hamilton populations (COHP): Energy-resolved visualization of chemical bonding in solids based on density-functional calculations. *J. Phys. Chem.* **1993**, *97*, 8617–8624. [CrossRef]
36. Maintz, S.; Deringer, V.L.; Tchougréeff, A.L.; Dronskowski, R. LOBSTER: A tool to extract chemical bonding from plane-wave based DFT. *J. Comput. Chem.* **2016**, *37*, 1030–1035. [CrossRef]
37. Momma, K.; Izumi, F. *VESTA*: A Three-Dimens. *Vis. Syst. Electron. Struct. Anal. J. Appl. Crystallogr.* **2008**, *41*, 653–658. [CrossRef]
38. Wang, V.; Xu, N.; Liu, J.C.; Tang, G.; Geng, W.T. VASPKIT: A user-friendly interface facilitating high-throughput computing and analysis using VASP code. *Comput. Phys. Commun.* **2021**, *267*, 108033. [CrossRef]
39. Nishihara, H.; Ono, K.; Neumann, K.U.; Ziebeck, K.; Kanomata, T. Complex magnetism in Fe_2VSi. *Phys. B Condens. Matter* **2003**, *329*, 1107–1108. [CrossRef]
40. Bertotti, G.; Ferchmin, A.; Fiorillo, E.; Fukamichi, K.; Kobe, K.; Roth, S. Magnetic alloys for technical applications. Soft magnetic alloys, Invar and Elinvar alloys. *Landolt Bornstein New Ser.* **1994**, *3*, 33–142.
41. Zamkova, N.; Zhandun, V.; Ovchinnikov, S.; Sandalov, I. Effect of local environment on moment formation in iron silicides. *J. Alloys Compd.* **2017**, *695*, 1213–1222. [CrossRef]
42. Draganyuk, O.N.; Zhandun, V.S.; Zamkova, N.G. Effect of the local environment on the magnetic properties of Mn_3Si: Hybrid ab initio and model study. *Phys. Status Solidi (B)* **2019**, *256*, 1900228. [CrossRef]
43. Draganyuk, O.N.; Zhandun, V.S.; Zamkova, N.G. Half-metallicity in Fe_2MnSi and Mn_2FeSi heusler compounds: A comparative ab initio study. *Mater. Chem. Phys.* **2021**, *271*, 124897. [CrossRef]
44. Aryal, A.; Bakkar, S.; Samassekou, H.; Pandey, S.; Dubenko, I.; Stadler, S.; Ali, N.; Mazumdar, D. Mn_2FeSi: An antiferromagnetic inverse-Heusler alloy. *J. Alloys Compd.* **2020**, *823*, 153770. [CrossRef]
45. Faleev, S.V.; Ferrante, Y.; Jeong, J.; Samant, M.G.; Jones, B.; Parkin, S.S. Origin of the tetragonal ground state of Heusler compounds. *Phys. Rev. Appl.* **2017**, *7*, 034022. [CrossRef]